RSC Advances

ROYAL SOCIETY OF CHEMISTRY

www.rsc.org/advances

In this work, a multifunctional drug delivery system was developed for potential application in NIR fluorescence imaging and targeting PDT.

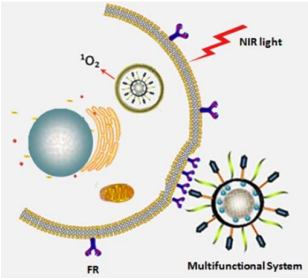

Journal Name RSCPublishing

ARTICLE

The multifunctional magnetic nanoparticles for simultaneous cancer near-infrared imaging and targeting photodynamic therapy †

Cite this: DOI: 10.1039/x0xx00000x

Received 00th January 2012,
Accepted 00th January 2012

DOI: 10.1039/x0xx00000x

www.rsc.org/

Xueling Zhao‡[a], Zongyan Chen‡[a], Hongli Zhao*[a], Denghao Zhang[a], Liang Tao[a], Minbo Lan*[a,b]

Cancer theranostics, the ability to simultaneous cancer diagnose and treatment, has become one of the major driving forces in nanobiotechnology. In the present work, a multifunctional system, methylene blue-incorporated folate-functionalized Fe_3O_4/mesoporous silica core/shell magnetic nanoparticles (MNPs), for simultaneous near-infrared (NIR) fluorescence imaging and targeting photodynamic therapy (PDT) has been developed. The core Fe_3O_4 MNPs offers the function of magnetically guided drug delivery, the mesoporous silica shell acts as an efficient drug loaded carrier, the photosensitizer methylene blue (MB) exhibits excellent NIR fluorescence imaging and PDT efficiency, and the folic acid (FA) can effectively enhance the delivery of MB to the targeting cancer cells which overexpress the folate receptor. The results indicated that the multifunctional system could effectively be used in NIR fluorescence imaging. Moreover, it exhibited a synergistic effect of magnetic targeted PDT of cancer under NIR laser irradiation. Thus, the multifunctional system is promising for simultaneous cancer diagnosis and therapy.

1 Introduction

Cancer is a devastating disease with incidence increasing at an alarming rate and survival not improved substantially during the past several decades. Although enormous efforts have been made in early detection and comprehensive treatment for this disease, little or no survival improvement was obtained, which needs further development of novel strategies.[1,2] According to the report from National Cancer Institute (NCI) in USA, nanobiotechnology, which not only carries multiple diagnostic/therapeutic payloads in the same package, but also facilitates the targeted delivery into specific sites and across complex biological barriers,[3] has tremendous potential for cancer prevention, diagnosis, imaging, and treatment.[4] The multifunctional integrated system combines different properties such as tumor targeting, imaging, and selective therapy in an all-in-one system, which will provide more useful multimodal approaches in the battle against cancer.[5-9]

Photodynamic therapy (PDT) is now well established as a technique for cancer treatment.[10-13] In contrast to other conventional medical treatments, PDT doesn't need to release the used drugs and it is based on the concept that photosensitizers (PSs) are able to generate reactive oxygen species (ROS) upon irradiation, such as singlet oxygen ($^1O_2$) or free radicals, and can irreversibly damage the pathological cells without damaging adjacent healthy ones.[14-16] Unfortunately, the phototoxicity, hydrophobicity and the low selectivity of the PS agents limit the current applications of PDT in cancer therapy.[17] Therefore, the development of new biocompatible delivery vehicle with stable aqueous dispersion, site-specific and time-controlled delivery abilities is still urgently needed. Among the various delivery vehicles, mesoporous silica nanoparticles (MSNs) hold the promise to be a highly efficient PDT drug delivery platform owing to their attractive features such as uniform pore size, large surface area and high accessible pore volume, ease of chemical modification, excellent biocompatibility and avid uptake by cells.[18-22] The porous structure of MSNs not only permits the accommodation of a large quantity of PSs, but also helps to enhance the permeability of oxygen and generate $^1O_2$, which is essential for PDT. Furthermore, their surfaces can be modified with special targeting moieties such as antibodies, folate and aptamers for site-specific behavior. However, to our knowledge, the application of multifunctional MSNs as photosensitizing vehicles that provides both MRI and fluorescence imaging diagnosis and photodynamic therapy has not been satisfied explored. There are very few reports available on the applications of MSNs as PSs vehicles.

Moreover, the accurate localization of PS-containing nanoparticles in cells or target tissues is very important for effective PDT. It will offer a powerful guidance for site-directed irradiation of target diseased tissues without causing

damage to the healthy tissues. Recently, optical imaging probes have been incorporated into MSNs along with PSs to offer dual capability of imaging and therapy.[23-25] Optical imaging can provide the highest sensitivity and obtain detailed information at subcellular levels, which allow accurate targeting and simultaneous phototherapy treatment. In fact, some PSs can emit fluorescence and generate $^1O_2$ simultaneously under the irradiation.[26] Methylene blue (MB) is a hydrophilic phenothiazinium photosensitizer with promising applications in the PDT for its high quantum yield of $^1O_2$ generation ($\Phi \sim 0.5$) in the excitation of the therapeutic window (600-900 nm), and low dark toxicity.[27,28] In addition, MB is also the most inexpensive of the commercially available near-infrared (NIR) fluorescent dyes, and has been widely used for bioanalysis.[29] Therefore, taking advantage of the intrinsic fluorescence of photosensitizer to develop single photosensitizer-encapsulated nanoparticles for simultaneous *in vivo* imaging and PDT is significant.

Enhancing tumor accumulation of therapeutic agents by physical forces such as an external magnetic field (MF) has emerged as a new tumor-targeting strategy. During this process, magnetic nanoparticles (MNPs) carrying therapeutics circulating in the bloodstream would be attracted by the MF applied on the tumor, resulting in greatly enhanced enrichment of therapeutic agents in targeted tumor region to improve the cancer treatment efficacy.[30] Moreover, MNPs as a magnetic resonance imaging (MRI) contrast agent exhibit a unique magnetic resonance (MR) contrast enhancement effect that enables noninvasive MRI of cell trafficking, gene expression, and cancer.[31,32]

Herein, in this paper, we present a core–shell structured nanomaterial, namely, Fe_3O_4@mSiO_2(MB)-FA, which is multifunctional in the fields of NIR fluorescence imaging and targeting PDT. The Fe_3O_4 nanoparticles were prepared *via* co-precipitation method, and mesoporous silica was coated as shell layer, in which photosensitizer was loaded. Then a layer of poly(ethylene glycol) (PEG) shell and folate receptors were synthesized. Systematic experiments *in vitro* and *in vivo* were designed to carefully evaluate the physical and chemical properties, cytotoxicity, cellular uptake, NIR light-induced cells killing, *in vivo* imaging, as well as targeting PDT of the multifunctional system (scheme 1).

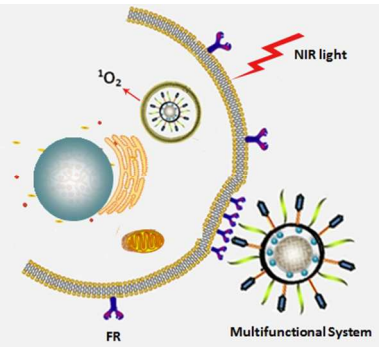

Scheme 1. The cancer cell targeting PDT mechanism of the multifunctional system.

2 Experimental

2.1 Materials

2.1.1 Reagents and materials. Ferric chloride hexahydrate ($FeCl_3$•$6H_2O$), ferrous chloride tetrahydrate ($FeCl_2$•$4H_2O$), sodium oleate ($C_{18}H_{33}ONa$), ammonium hydroxide (25%, aqueous solution), tetraethoxysilane (TEOS), ammonium nitrate (NH_4NO_3), cetyltrimethylammonium bromide (CTAB), 3-amino-propyltriethoxysilane (APTES), Methylene blue (MB), folic acid (FA), 1-ethyl-3[3-dimethylaminopropyl] carbodiimide hydrochloride (EDC), dicyclohexylcarbodiimide (DCC), dimethyl sulfoxide (DMSO) and N-hydroxysuccinimide (NHS) were obtained from Sinopharm Chemical Reagent Co. Ltd., and used without further purification. 2-methoxy (polyethyleneoxy) propyltrimethoxysilane (PEG–silane) was from Gelest (USA). 3-(4, 5-dimethylthiazol-2-yl)-2, 5-diphenyltetrazolium bromide (MTT), 4, 6-diamidino-2-phenylindole (DAPI) and DPBF were purchased from Sigma–Aldrich (USA). Dulbecco's modified Eagle's medium (DMEM) cell culture medium, penicillin, streptomycin, trypsin, fetal bovine serum (FBS), and heparin sodium were bought from Gibco Invitrogen (USA). All other chemicals and reagents were of analytical grade and used as received.

2.1.2 Cell lines and animal. Human ovarian cancer cells (SK-OV-3 cells), human cervical cancer cells (HeLa cells), mouse sarcoma cells (S-180 cells) and mouse fibroblast cells (NIH 3T3 cells) were purchased from the Shanghai Institutes for Biological Sciences, Chinese Academy of Sciences (Shanghai, China). Kunming mice of clean grade (female, 4-6 weeks old) and BALB/c mice (female, 4-6 weeks old, 16-18 g of body weight) were purchased from Shanghai SLAC Laboratory Animal Center (Shanghai, China), and were used in accordance with approved institutional protocols established by the Shanghai Department of Experimental Animals Management.

2.2 Methods

2.2.1 Synthesis of Fe_3O_4@mSiO_2(MB)-FA nanoparticles. Fe_3O_4@mSiO_2(MB)-FA nanoparticles were synthesized following the method in our previous report.[33] Firstly, highly biocompatible monodisperse superparamagnetic Fe_3O_4@mSiO_2 core/shell nanoparticles with mesoporous silica shells were synthesized. Then these particles were coated with the covalently bonded biocompatible polymer PEG and modified with the cancer targeting ligand FA. Finally, the water-soluble photosensitizer MB was loaded into the mesoporous silica shell.

2.2.2 Characterization of Fe_3O_4@mSiO_2(MB)-FA nanoparticles. The particles were characterized by means of powder X-ray diffraction (XRD), transmission electron microscopy (TEM), dynamic light scattering (DLS), Fourier transformed infrared spectroscopy (FT-IR), Brunauer-Emmett-Teller (BET), vibrating sample magnetometer (VSM), UV-Vis and fluorescence spectroscopy. High-resolution TEM data were

collected on a JEOL model JEM 2100 electron microscope operating at an accelerating voltage of 200 kV. DLS data were obtained on an electrophoretic light scattering spectrophotometer (Beckman Coulter Delsa nano C, USA). XRD data were collected on a Rigaku corporation D/MAX 2550 VB/PC Multi-Purpose X-ray diffractometer with Cu Kα radiation (λ= 0.1542 nm). The specific surface area was calculated by the BET (ASAP 2020-M) method. The pore size distribution was obtained from the Barret-Joner-Halenda (BJH) method. The FT-IR spectra of the nanoparticles were obtained on a Nicolet 6700 spectrometer. Magnetic properties were recorded using a VSM (Lake Shore, USA). UV-Vis absorption spectra were measured on an UV-Vis Spectrophotometer (Evolution 220, Japan). Fluorescence spectra of liquid state were recorded on a Lumina Fluorescence spectrometer. (Thermo scientific, USA). The cellular images were acquired with a confocal laser scanning microscope (CLSM, Nikon AIR).

2.2.3 Detection of singlet oxygen. Commonly, there are two methods for the detection of $^1O_2$, one the method by using luminescence emission spectra at 1270 nm,[34-36] the second is based on an indirect method using a chemical $^1O_2$ probe.[36,37] In this study, DPBF is used as a probe[34,37] to detect the $^1O_2$ quantum yield. DPBF reacts irreversibly with $^1O_2$ that causes a decrease in the intensity of the DPBF absorption band at 400 nm. In a typical experiment, 15 mL of DPBF in acetonitrile (5.5 mM) was mixed with 2 mL, 1.5 mg/mL of Fe_3O_4@mSiO_2(MB)-FA nanoparticles in acetonitrile. The experiment mixed DPBF with free MB dispersed in acetonitrile used as the standard. The solutions were irradiated with a 650 nm laser source at 5 mW/cm^2, and their absorbencies at 400 nm were recorded at every 10 seconds, using a UV-Vis Spectrophotometer.

2.2.4 Cytotoxicity assessment. The *in vitro* cytotoxicity was measured by using the MTT assay in SK-OV-3 cells. Cells (1×10^5 well^{-1}) were inoculated into a 96-well cell-culture plate and then incubated at 37 ^{o}C in a 5% CO_2-humidified incubator for 24 h. 200 μL of Fe_3O_4@mSiO_2(MB)-FA nanoparticles with different concentrations (10-200 μg/mL), DMEM were added to the wells, separately. After incubation for 24 h and 48 h at 37 ^{o}C under 5% CO_2, the supernatant was removed. Subsequently, MTT (20 μL, 5 mg/mL) solved in DMEM (200 μL) were added and the plates were incubated at 37 ^{o}C for another 4 h. Then supernatant was removed before DMSO was added to each well to dissolve the formazan. The absorbance at 492 nm and 630 nm was detected with spectrophotometric microplate reader (THERMO Multiskan MK3 spectrometer). Each data point was collected by averaging that of three wells, and the untreated cells were used as controls. The following equation was used to calculate the inhibition of cell viability.

$$\text{Cell viability}(\%) = \left(\frac{\text{mean absorption of value treatment group}}{\text{mean absorption value of control}}\right) \times 100\%$$

2.2.5 Cellular uptake study. The cellular uptake and distribution of Fe_3O_4@mSiO_2(MB)-FA nanoparticles were performed using flow cytometry and CLSM. For flow cytometry, HeLa cells (1×10^6) that overexpress folate receptors were seeded in 6-well culture plates and cultured for 24 h. Following this, the cells were treated with Fe_3O_4@mSiO_2(MB)-FA nanoparticles (200 μg/mL) for 2 h and 4 h. After the preset time intervals, the culture medium was discarded, and cells were washed three times with PBS and harvested with trypsinization. The cell pellets were resuspended in PBS and measured for the fluorescence intensity (excitation: 650 nm; emission: 690 nm) on a BD FACSAria flow cytometer (Beckton Dickinson，USA), and Cell Quest software was used to analyze the data.

For CLSM studies, HeLa cells were propagated in DMEM containing FBS (10%) and penicillin/streptomycin (1%). Then the cells were digested and resuspended in the DMEM medium (without FARs). 1×10^4 cells were transferred into a 6-well tissue culture plates. After 24 h of incubation, the cells were carefully rinsed with PBS (pH 7.4). 2 mL DMEM medium of the Fe_3O_4@mSiO_2(MB)-FA (200 μg/mL) were added to the Petri dishes and incubated for 2 h, followed by three-time rinses with PBS. After fixation with 4% paraformaldehyde in PBS at room temperature for 30 min and then cells were treated with 1 mL 0.01% Triton X-100 (Sigma) for 10 min and the nuclei were stained with DAPI (1 μg/mL, Sigma) for 15 min. Each step of the above was washed with PBS three times. Then cover slips containing cells were mounted onto slides and were then observed under CLSM.

2.2.6 *In vitro* PDT effect. Two 96-well plates were divided into two groups: dark control and experimental group. SK-OV-3 cells were seeded in the 96-well plate at a density of 1×10^4 cells per well for 24 h. Then DMEM cell medium containing different concentrations of Fe_3O_4@mSiO_2(MB)-FA nanoparticles were added to the wells (200 μL per well, 0, 10, 50, 100, 150, 200 μg/mL). After incubation for 24 h, the cells were washed three times with 200 μL PBS to remove the unbound nanoparticles. Then 200 μL PBS was added and the cells were exposed to a 650 nm laser with a power density of 70 mW/ cm^2 for 4 min. After irradiation, cells were incubated another 24 h in a 5% CO_2, 95% air humidified incubator at 37 ^{o}C. Dark control group keeps identical to experimental group without irradiation. The cell viability was measured by a MTT assay mentioned above and expressed as a percentage of the control.

2.2.7 *In vivo* imaging of Fe_3O_4@mSiO_2(MB)-FA nanoparticles in animals. The female BALB/c mice were maintained in a pathogen-free condition on arrival. To generate HeLa tumor xenografts, 1×10^7 cells suspended in 200 μL of salined were subcutaneously implanted into the right limb armpits of the mice. Tumors were allowed to grow until the average volume of the xenograft tumors was approximately 50 mm^3 (about 10 days). The mice were randomly divided into three groups, three mice each group. For group I, the mice were administrated with saline; group II, Fe_3O_4@mSiO_2(MB)-NH_2; group Ⅲ, Fe_3O_4@mSiO_2(MB)-FA. Fe_3O_4@mSiO_2(MB)-NH_2 and Fe_3O_4@mSiO_2(MB)-FA administrated were 5 mg MB equiv/kg through tail vein in all of the formulations. The whole body *in vivo* fluorescence imaging of the mice was performed

an hour later utilizing a *In-Vivo* Imaging System IVIS Lumina II (Coliper, USA). The instrument equipped with fluorescent filter sets (excitation/emission wavelength of 650/690 nm).

2.2.8 *In vivo* anti-tumor properties. Xenograft tumor mouse model. All animal experiments were performed under a protocol approved by Shanghai laboratory animal center. Mice ascitic tumor models were generated by subcutaneous injection of 1×10^6 S-180 cells in 0.1 mL saline into the right armpit of female Kunming mice (18-22 g, Shanghai SLAC Laboratory Animal Center). The mice were used when the tumor volume reached 50×50 mm^3.

In vivo PDT. For the *in vivo* antitumor experiments, the tumor-bearing mice were divided into five groups (n=5), minimizing the differences of weights and tumor sizes in each group. The mice were administered with (1) saline, (2) magnetic/650 nm laser, (3) Fe_3O_4@mSiO_2(MB)-FA/650 nm laser, (4) Fe_3O_4@mSiO_2(MB)-FA/magnetic, (5) Fe_3O_4@mSiO_2(MB)-FA/magnetic/650 nm laser, (Fe_3O_4@mSiO_2(MB)-FA dose: 5 mg/kg) in saline were intravenously injected into mice *via* the tail vein every 2 days, respectively, and then the tumor regions were irradiated with 650 nm laser (70 mW/cm^2, 10 min) at 4 h post-injection. For the purpose of *in vivo* magnetic targeting, a magnet was glued onto the tumor site of the mice. The mice were observed daily for clinical symptoms and the tumor sizes were measured by a caliper every 24 h.

2.2.9 Statistical analysis. Data were analyzed using the SPSS software package. Quantitative data are expressed as mean ± SD and analyzed by use of Student' s t test. P values < 0.05 were considered statistically significant.

3 Results and discussion

3.1 Synthesis and characterization of Fe_3O_4@mSiO_2(MB)-FA

In our experiments, the multifunctional Fe_3O_4@mSiO_2(MB)-FA nanoparticles were prepared by a multistep process (see Methods section for details in our previous report[37]). The TEM image displayed in Fig. S1 (A) shows that the prepared hydrophobic Fe_3O_4 are monodispersed nanoparticles with a uniform average diameter of 5 nm. The MB-loaded Fe_3O_4@mSiO_2-FA nanoparticles are discrete and uniform with an average diameter of 70 ± 5 nm, and well-ordered mesopores were also clearly observed (Fig. 1S (B)). In addition, the DLS data (Fig. S2) shows Fe_3O_4@mSiO_2(MB)-FA has narrow size distribution with an overall hydrodynamic diameter of 89.8 nm in water without aggregation. The crystallinity of Fe_3O_4 does not change after modification of FA and load of MB (Fig. S3). Moreover, the uniform mesoporous pore size along with small particle size (<100 nm) are facilitative and favorable for drug delivery applications (Fig. S4). The representative hysteresis loop of Fe_3O_4@mSiO_2(MB)-FA at ambient temperature are shown in Fig. S5, and the saturation magnetization of the Fe_3O_4@mSiO_2(MB)-FA is ~8.46 emu/g, which suggested the superparamagnetism of the as-prepared nanoparticles.

3.2 Singlet oxygen detection

In this study, the $^1O_2$-generation capability of the Fe_3O_4@mSiO_2(MB)-FA nanoparticles was assessed using DPBF, a $^1O_2$ chemical probe, in acetonitrile under 650 nm laser irradiation (5 mw/cm^2). DPBF reacts irreversibly with $^1O_2$ and the reaction can be followed by recording the decrease in the intensity of the DPBF absorption at around 400 nm. The changes in the absorption spectra of DPBF in the presence of Fe_3O_4@mSiO_2(MB)-FA nanoparticles after different irradiation times are shown in Fig. 5. Control tests were carried out to confirm that the decrease in the absorption of DPBF was induced by $^1O_2$ (Fig. 1, inset). In the presence of Fe_3O_4@mSiO_2(MB)-FA nanoparticles, the DPBF absorption at 400 nm dramatically decreases under NIR-laser irradiation (Fig. 1, curve a in the inset), thereby suggesting that these nanoparticles are highly efficient in the generation of reactive $^1O_2$. In contrast, there are fewer decreases in DPBF absorbance for free MB (Fig. 1, curve b in the inset). The effective $^1O_2$-generating capability of our nanoparticles under NIR light makes it possible for them to be applied in NIR-induced PDT.

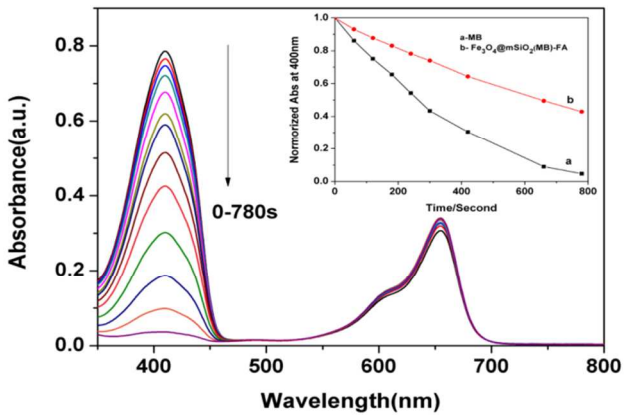

Fig. 1. Absorption spectra of Fe_3O_4@mSiO_2(MB)-FA in the presence of DPBF after different times of irradiation with a 650 nm laser source at 5 mw/cm^2. Inset: Decay curves of absorption of DPBF as function of time of irradiation. DPBF with dispersion of Fe_3O_4@mSiO_2(MB)-FA (a) and DPBF with MB free (b) in acetonitrile.

3.3 Cellular uptake

The ability to target nanoparticles to specific organelles or receptors is one of the most important factors for their prospective application in bioimaging and drug delivery. Various types of targeting agents, such as antibodies, aptamers and FA, have been developed for the specific identification antigens or receptors on targeting cancer cells. In this study, FA was modified onto the Fe_3O_4@mSiO_2 as the targeting component because folate receptors (FR) are overexpressed in many human cancerous cells.

Flow cytometry and CLSM were used to evaluate the effect of FA on the celluar uptake behavior of Fe_3O_4@mSiO_2(MB)-FA against FR positive HeLa cells. To precisely observe the cellular distributions of the multifunctional nanoparticles, the double fluorescence–labeling experiments and visualized red fluorescence from MB and blue fluorescence from DAPI

labeling the nucleus were performed. As described in Fig. S6, intense red fluorescence of MB loaded Fe_3O_4@mSiO_2-FA is observed in the cytoplasm of FA-positive HeLa and SK-OV-3 cells in comparison with NIH 3T3 cells without folate receptors, whose fluorescence could be negligible. The results confirm that objective of increasing specificity and sensitivity of Fe_3O_4@mSiO_2(MB)-FA image by labeling cancer cells with over-expression of folate receptors on the surface has been achieved. And with the increase of the incubation time, the red fluorescence in both cytoplasm and nuclei increased (Fig. 2).

The cellular uptake of Fe_3O_4@mSiO_2(MB)-FA into HeLa cells was futher quantitatively analyzed with flow cytometry. Fig. 3A shows the flow cytometry histograms of MB fluorescence from HeLa cells incubated with Fe_3O_4@mSiO_2(MB)-FA with the concentration of 200 μg/mL for 2 h and 4 h, respectively. Cells without any treatment were used as a negative control to detect autofluorescence. The flow cytometry analysis clearly demonstrated that the changes in fluorescence intensity of MB were observed in the cells after 2 h incubation with Fe_3O_4@mSiO_2(MB)-FA. With the increase of the incubation time, the relative geometrical mean fluorescence intensity of Fe_3O_4@mSiO_2(MB)-FA pretreated cells obvious increases (Fig. 3B).

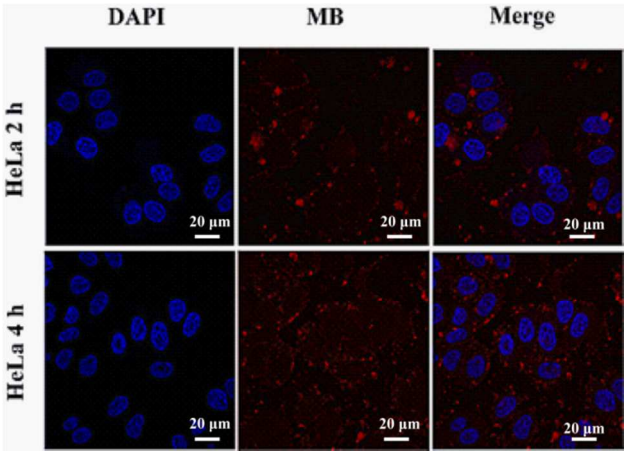

Fig. 2. Confocal laser micrographs of HeLa (D, E, F) cells incubated with Fe_3O_4@mSiO_2(MB)-FA for 2 h and 4 h. For each panel, from left to right were the cells with unclear staining with DAPI, with MB fluorescence and overlays of images.

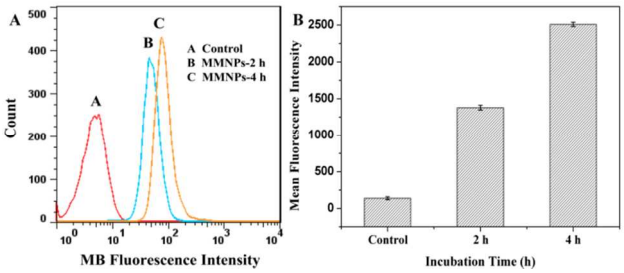

Fig. 3. Flow cytometry histogram profiles (A) and fluorescence intensity (B) of HeLa cells after incubation with Fe_3O_4@mSiO_2(MB)-FA nanoparticles for 2 h and 4 h.

3.4 Laser induced *in vitro* PDT effects on cancer cells

In order to assess the dark cytotoxicity of our multifunctional Fe_3O_4@mSiO_2(MB)-FA nanoparticles for *in vivo* applications, we did an MTT assay using SK-OV-3 cells as model and the results indicate that Fe_3O_4@mSiO_2(MB)-FA displays non-cytotoxicity and good biocompatibility on SK-OV-3 cells within 0-200 μg/mL (Figure S7). To investigate the PDT efficiency of Fe_3O_4@mSiO_2(MB)-FA, SK-OV-3 cells were first incubated with different concentrations of Fe_3O_4@mSiO_2(MB)-FA for 24 h and then treated with/without laser (650 nm) irradiation. The MTT assay was used to evaluate the cell viabilities. Cell viability was normalized to control cells (no drug and nonirradiated). The combination of 24 h exposure of tumor cells to Fe_3O_4@mSiO_2(MB)-FA followed by laser irradiation-induced dose and light-dependent cytotoxicity on the tumor cells, which was significantly different from non-irradiation control in statistics, as shown in Fig. 4A and Fig. 4B. With the increase of drug dose and light dose, the cell viability gradually decreases. To the irradiated group, 100 μg/mL Fe_3O_4@mSiO_2(MB)-FA causes approximately 50% cell viability lost, demonstrating an obvious photodynamic activity. When the concentration of Fe_3O_4@mSiO_2(MB)-FA reaches 200 μg/mL, the cells are almost death (about 80% loss of cell viability). The group treated with the drug without light exposure shows that the drug alone has no effects on tumor cells which coincides with the result of cytotoxicity assessment.

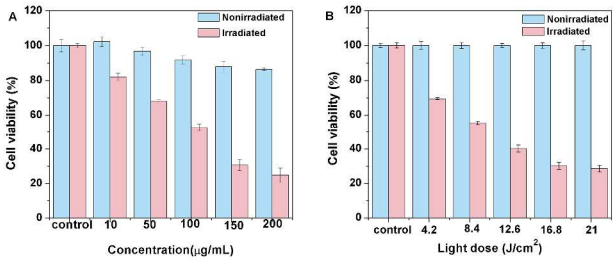

Fig. 4. Phototoxicity of Fe_3O_4@mSiO_2(MB)-FA to HeLa cells. (A) SK-OV-3 cells were incubated with 0-200 μg/mL Fe_3O_4@mSiO_2(MB)-FA for 24 h at 37 °C in the dark prior to irradiation for 4 min with 650 nm laser (70 mW/cm^2). (B) SK-OV-3 cells were incubated with 150 μg/mL Fe_3O_4@mSiO_2(MB)-FA for 24 h at 37 °C in the dark prior to of a series of light doses (0, 4.2, 8.4, 12.6, 16.8 and 21 J/cm ^{2}).

3.5 *In vivo* imaging

The tumor uptake of Fe_3O_4@mSiO_2(MB)-FA in the mice was determined by NIR fluorescence imaging of cancer tumor model mice after injection of nanoparticles *via* the tail vein. Figure 5 shows *in vivo* near infrared fluorescence imaging of saline (Fig. 5I), Fe_3O_4@mSiO_2(MB)-NH_2 (Fig. 5 Ⅱ) and Fe_3O_4@mSiO_2(MB)-FA (Fig. 5Ⅲ) in mice after 1.5 h, 3 h and 4.5 h post-injection through the tail vein. As expected, from Fig. 5, Fluorescence signal in mouse Ⅲ (A, B, C) distributed throughout the whole body, and the intensity of mouse Ⅲ (A, B, C) was higher than that of mouse Ⅱ (A, B, C) at the tumor site. The results indicated that Fe_3O_4@mSiO_2(MB)-FA exhibited a longer plasma circulation time than others. However, Fe_3O_4@mSiO_2(MB)-NH_2 in blood decreased rapidly after the

intravenous administration due to the fact that Fe_3O_4@mSiO_2(MB)-FA reduced the uptake of MB by the reticuloendothelial system (RES) and the mononuclear phagocyte system.[23] In the images of *ex vivo* (Figure 5D), the high accumulation of nanoparticles was observed in RES organs, including liver, spleen and kidney, possibly caused by the clearance of the RES. And a significant enhance in MB levels was found in tumor site of mouse Ⅲ, indicating that the FA conjugated nanoparticles are able to be recognized by the FR of tumor cells. The prolonged circulation gave the opportunity for Fe_3O_4@mSiO_2(MB)-FA to accumulate to the tumor site by EPR effect and made FA conjugated nanoparticles contact with tumor cells and internalize into the tumor cell *via* receptor-mediated endocytosis.

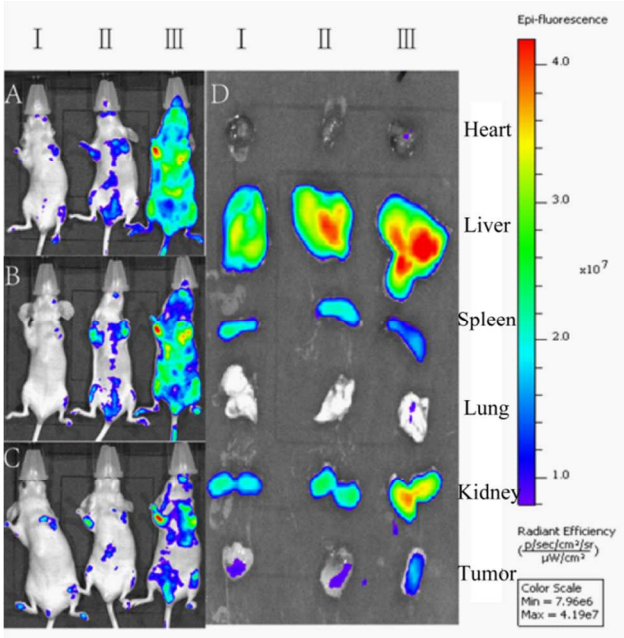

Fig. 5. *In vivo* optical fluorescence imaging of HeLa tumor xenografted mude mice and their several organs and tumor, which were taken after sacrifice (at 4.5 h post-injection)

3.6 *In vivo* antitumor efficacy

To investigate *in vivo* PDT efficacy of Fe_3O_4@mSiO_2(MB)-FA, comparative efficacy studies were conducted. The S-180 tumor-bearing mice were divided into 5 groups and were treated according to protocols as summarized in method Section 2.2.9. The changes of relative tumor volume as a function of time were plotted in (Fig. 6A). After 8 days treatment, control group shows a relative tumor volume (V/V_0) of 8.70 ± 0.89, Magnet/650 nm laser and Fe_3O_4@mSiO_2(MB)-FA/magnet results in V/V_0 of 9.53 ± 0.96 and 8.79 ± 0.67, the tumor-bearing mice treated with Fe_3O_4@mSiO_2(MB)-FA/650 nm laser and Fe_3O_4@mSiO_2(MB)-FA/magnet/650 nm laser achieves (V/V_0) of 6.11 ± 0.6 and 5.45 ± 0.95. Fe_3O_4@mSiO_2(MB)-FA/magnet/650 nm laser has tumor growth inhibition (TGI) of 62.64%, it is significantly more effective than the other therapeutic groups ($p < 0.05$). In Figure 6B and Figure 6C, it was obvious that, compared with control group, mice treated with Fe_3O_4@mSiO_2(MB)-FA/650 nm laser, the tumor volume is greatly reduced, this is a successful application that MB is used as a photosensitizer in PDT to achieve *in vivo* tumor treatment efficacy. Remarkably enhanced PDT effect is observed for tumor-bearing mice treated by Fe_3O_4@mSiO_2(MB)-FA/magnet/650 nm laser, in comparison to that treated with Fe_3O_4@mSiO_2(MB)-FA/650 nm laser at the same Fe_3O_4@mSiO_2(MB)-FA and light doses. Because of the magnetic targeting property of Fe_3O_4@mSiO_2(MB)-FA, when a magnet is glued to the top of the tumor, more Fe_3O_4@mSiO_2(MB)-FA will go to the tumor site than non-magnetic group, so the PDT efficacy of Fe_3O_4@mSiO_2(MB)-FA with a magnet is higher than that of non-magnetic group. The growth of tumor tissue is successfully suppressed by Fe_3O_4@mSiO_2(MB)-FA/magnet/650 nm laser. This high therapeutic efficacy originates from the high Fe_3O_4@mSiO_2(MB)-FA accumulation in tumor tissue.

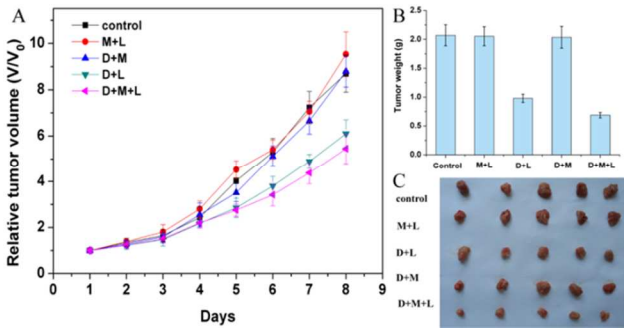

Fig. 6. Antitumor efficacy of Fe3O4@mSiO2(MB)-FA in the Kunming mice bearing S-180 tumors at a dose of 5 mg/kg; each group was intravenously administered every day for a total of 8 times, error bars were based on SD of five tumors per group. Control: blank; M: magnet; D: drug; L: light. A: Tumor growth of mice in different treatment groups within 8 days. B: Quantitative results of tumor weight excised from the tumor-bearing mice sacrificed on day 8. C: The picture of the tumors in different groups at the end of the experiment.

Conclusions

In summary, a multifunctional system Fe_3O_4@mSiO_2(MB)-FA for simultaneous cancer NIR imaging and targeting PDT is successfully designed and developed. The prepared Fe_3O_4@mSiO_2(MB)-FA has high water-solubility, non-cytotoxicity, good biocompatibility, and can serve as a powerful PDT agent for *in vitro* fluorescence imaging and PDT cancer cell killing under NIR light irradiation. *In vivo* targeting PDT is further demonstrated in our animal experiments, showing excellent tumor ablation therapeutic efficacy by using Fe_3O_4@mSiO_2(MB)-FA as the targeting PDT agent. Consequently, this unique multifunctional system may have great potential application in early diagnosis and therapy of cancer.

Acknowledgements

This research was financially supported by the Science and Technology Commission of Shanghai Municipality (STCSM, contract Nos. 13ZR1412000 and 12nm0501100).

Notes and references

[a] Shanghai Key Laboratory of Functional Materials Chemistry, and Research Centre of Analysis and Test, East China University of Science and Technology, Shanghai 200237, P. R. China

[b] State Key Laboratory of Bioreactor Engineering, East China University of Science and Technology, Shanghai 200237, P. R. China

Corresponding authors. E-mail: honglizhao@ecust.edu.cn; (Dr. Hongli Zhao) minbolan@ecust.edu.cn; (Prof. Dr. Minbo Lan) Tel: +86-21-64253574; Fax: +86-21-64252947

† Electronic Supplementary Information (ESI) available: [Additional information includes the characterizations by TGA and TEM of samples; supporting figures of cytotoxicity assessment and cellular uptake]. See DOI: 10.1039/b000000x/

‡ These authors contributed equally to this work.

references

1. F. Yang, C. Jin, S. Subedi, C. L. Lee, Q. Wang, Y. J. Jiang, J. Li, Y. Di and D. L. Y, *Cancer. Treat. Rev.*, 2012, **38**, 566-579.
2. B. Sivakumar, R. G. Aswathy, Y. Nagaoka, S. Iwai, K. Venugopal, K. Kato, Y. Yoshida, T. Maekawa and D. N. Sakthi Kumar, *RSC Advances*, 2013, **3**, 20579-20598.
3. A. C. Bonoiu, S. D. Mahajan, H. Ding, I. Roy, K. T. Yong, R. Kumar, R. Hu, E. J. Bergey, S. A. Schwartz and P. N. Prasad, *Proc. Natl. Acad. Sci. USA*, 2009, **106**, 5546-5550.
4. A. Jemal, R. Siegel, E. Ward, Y. P. Hao, J. Q. Xu, T. Murray and M. J. Thun, *CA-Cancer J. Clin.*, 2008, **58**, 71-96.
5. O. C. Farokhzad, J. Cheng, B. A. Teply, I. Sherifi, S. Jon, P. W. Kantoff, J. P. Richie and R. Langer, *Proc. Natl. Acad. Sci. U S A*, 2006, **103**, 6315-6320.
6 . K. Yan, P. Li, H. Zhu, Y. Zhou, J. Ding, J. Shen, Z. Li, Z. Xu and P.K. Chu, *RSC Adv.*, 2013,**3**, 10598-10618
7. Z. H. Cao, R. Tong, A. Mishra, W. C. Xu, G. C. L. Wong, J. J. Cheng and Y. Lu, *Angew. Chem. Int. Edit.*, 2009, **121**, 6616-6620.
8. J. Kim, H. S. Kim, N. Lee, T. Kim, H. Kim, T. Yu, I. C. Song, W. K. Moon and T. Hyeon, *Angew. Chem. Int. Ed.*, 2008, **47**, 8438 –8441.
9. X. Z. Shi, H. Gong, Y. J. Li, C. Wang, L. Cheng and Z. Liu, *Biomaterials*, 2013, **34**, 4786-4793.
10. D. Bechet, P. Couleaud, C. Frochot, M. L. Viriot, F. Guilleminand and M. Barberi-Heyob, *Trends. Biotechnol.,* 2008, **26**: 612-621.
11. Y. N. Konan, R. Gurny and E. Allemann, *J. Photoch. Photobio. B*, 2002, **66**, 89-106.
12. S. B. Brown, E. A. Brown and I. Walker, *Lancet. Oncol.,* 2004, **5**, 497-508.
13. A. Mazzaglia, C. Conte, A. Scala, G.Siracusano, N. Leone, S. Patanè, F. Ungaro, A. Miro, M. T. Sciortino and F. Quaglia, *RSC Adv.*, 2014, DOI: 10.1039/C4RA07847K.
14. P. Couleaud, V. Morosini, C. Frochot, S. Richeter, L. Raehmand and J.O. Durand, *Nanoscale*, 2010, **2**, 1083–1095.
15. R. R. Allison, R. E. Cuenca, G. H. Downie, P. Camnitz and B. Brodish, *Photodiagn. Photodyn.*, 2005, **2**, 205-222.
16. Z. W. Li, C. Wang, L. Cheng, H. Gong, S. N. Yin, Q. F. Gong, Y. Q. Li and Z. Liu, *Biomaterials*, 2013, **34**, 9160-9170.
17. Y. Cheng, J. D. Meyers, A. M. Broome, M. E. Kenney, J. P. Basilion and C. Burda, *J. Am. Chem. Soc.*, 2011, **133**, 2583-2591.
18. B. I. Slowing, B. G. Trewyn, S. Giri and VS-Y. Lin, *Adv. Funct. Mater.*, 2007, **17**, 1225-1236.
19. M. Gary-Bobo, O. Hocine, D. Brevet, M. Maynadier, L. Raehm, S. Richeter, V. Charasson, B. Loock, A. Morère, P. Maillard, M. Garcia and J. O. Durand, *Int. J. Pharm.,* 2012, **423**, 509-515.
20. J. Wang, C.K. Tsung, R. C. Hayward, Y. Wu and G. D. Stucky, *Angew. Chem. Int. Edit.*, 2005, **44**, 332-336.
21. J. Lu, M. Liong, J. I. Zink and F. Tamanoi, *Small*, 2007, **3**, 1341-1346.
22. S. L. Gai, P. P. Yang, C. X. Li, W. X. Wang, Y. L. Dai, N. Niu and J. Lin, *Adv. Funct. Mater.*, 2010, **20**, 1161-1172.
23. S. H. Cheng, C. H. Lee, M. C. Chen, J. S. Souris, F. G. Tseng, C. S. Yang, C. Y. Mou, C. T. Chen and L. W. Lo, *J. Mater. Chem.*, 2010, **20**, 6149-6157.
24. A. K. Parchur, A. A. Ansari, B. P. Singh, T. N. Hasan, N. A. Syed, S. B. Rai and R. S. Ningthoujam, *Integr. Biol.*, 2014, 6, 53—64.
25. A. A. Ansari, T. N. Hasan, N. A. Syed, J. P. Labis, A.K. Parchur, G. Shafi, A. A. Alshatwi, *Nanomedicine*, 2013, 9, 1328–1335.
26. N. Nishiyama, Y. Morimoto, W.D. Jang and K. Kataoka, *Adv. Drug. Deliver. Rev.*, 2009, **61**, 327-338.
27. R. Dabestani and I. N. lvanov, *Photochem. Photobiol.*, 1999, **70**, 10-34.
28. S. H. Seo, B. M. Kim, A. Joe, H. W. Han, X. Chen and Z. Cheng, *Biomaterials*, 2014, **35**, 3309-3318.
29. T. Deng, J.S. Li, J.H. Jiang, G.L. Shen and R.Q. Yu, *Adv. Funct. Mater.,* 2006, **16**, 2147-2155.
30. Y. Chen, H. Chen, S. Zhang, F. Chen, S. Sun, Q. He, M. Ma, X. Wang, H. Wu, L. Zhang, J. Shi, *Biomaterials*, 2012, **33**, 2388-2398.
31. B. P. Pan, D. X. Cui, Y. Sheng, C. Ozkan, F. Gao, R. He, Q. Li, P. Xu and T. Huang, *Cancer Res.*, 2007, **67**, 8156-8163.
32. F. Hu, L. Wei, Z. Zhou, Y. Ran, Z. Li and M. Gao, *Adv. Mater.*, 2006, **18**, 2553-2556.
33. X. L. Zhao, H. L. Zhao, Z. Y. Chen, D. H. Zhang and M. B. Lan, *J. Nanosci. Nanotechnol*, 2014；DOI: 10.1166/jnn.2014.9867.
34. P. K. Frederiksen, M. Jørgensen and P. R. Ogilby, *J. Am. Chem. Soc.*, 2001, **123**, 1215-1221.
35. A. Karotki, M. Kruk, M. Drobizhev, A. Rebane, E. Nickel and C. W. Spangler, *J. Sel. Top. Quant.*, 2001, **7**, 971-975.
36. W. Spilleer, H. Kliesch, D. Wohrle, S. Hackbarth, B. R. B. Roder and G. Schnurpfeil, *J. Porphyr. Phthalocya.*, 1998, **2**, 145-158.
37. X. L. Zhao, H. L. Zhao, H. H. Yuan and M. B. Lan, *J. Biomed. Nanotechnol.*, 2014, **10**, 262-270.